Numerical analysis of fracture propagation during hydraulic fracturing operations in shale gas systems

Jihoon Kim [a,b,*], George J. Moridis [a]

[a] Earth Sciences Division, Lawrence Berkeley National Laboratory, 1 Cyclotron Road 74R316C, Berkeley, CA 94720, USA
[b] Harold Vance Department of Petroleum Engineering, Texas A&M University, 3116 TAMU 407 K Richardson Building College Station, TX 77843, USA

ABSTRACT

We perform numerical studies on vertical fracture propagation induced by tensile hydraulic fracturing for shale gas reservoirs. From the numerical simulation, we find that tensile fracturing occurs discontinuously in time, which generates saw-toothed responses of pressure, the fracture aperture, and displacement, and that fracture propagation is sensitive to factors such as initial condition of saturation, a type of the injection fluid, heterogeneity, tensile strength, elastic moduli, and permeability models. Gas injection induces faster fracturing in shale gas reservoirs than water injection, for the same mass injection, because of high mobility of gas. However, water injection to highly water-saturated formations can contribute to fast pressurization and high mobility of water, resulting in large fracturing. For moderate initial water saturation, complex physical responses within the fracture result from strong nonlinear permeability and multiphase flow with gravity.

Pressure diffusion and pressurization within the fracture are also affected by permeability. High intrinsic and high relative permeabilities result in fast fluid movement of injected fluid, followed by fast fracturing. High Young's modulus and high Poisson's ratio do not seem favorable to fracture propagation, although they are not significantly sensitive. For heterogeneity, a geological layer of high strength between near surface and above the shale gas reservoirs can prevent vertical fracture propagation, changing the direction of fracturing horizontally.

© 2015 Elsevier Ltd. All rights reserved.

1. Introduction

The potential natural gas resource from shale gas is estimated between 14.16×10^{12} m^3 and 28.3×10^{12} m^3, and, from its huge quantity, shale gas has been taken as one of the future energy resources [1,2]. For example, abundant shale gas in the U.S is found in Barnett Shale, Haynesville/Bossier Shale, Antrim Shale, Fayetteville Shale, New Albany Shale, and Marcellus Shale [3]. Despite abundance of the shale gas, geological formations of shale gas are extremely low permeable [4], and thus the shale gas reservoirs are considered unconventional resources.

Hydraulic fracturing has been introduced to production of the shale gas reservoirs in order to enhance permeability, creating artificial fractures within extremely low permeable formations [5,6]. Horizontal wells along with hydraulic fracturing are operated in order to increase productivity of gas production [7,8]. The horizontal wells and hydraulic fracturing techniques made gas production from Barnett shale successful, and the success has led to gas production of other shale reservoirs such as Marcellus shale, one of the largest natural gas resources in the United States [1,9].

Many studies have been made on hydraulic fracturing and shale gas reservoirs. Vermylen and Zoback [5] investigated two different scenarios for hydraulic fracturing along horizontal wells: alternatively fractured (zipperfrac) and simultaneously fractured (simulfrac) wells, and they found significant differences in stimulation for the two fracturing procedures. Fisher and Warpinski [6] analyzed fracture propagations induced by hydraulic fracturing with real geophysical field data, and concluded that the fracture propagations were limited in the vertical direction, compared with the horizontal direction. They claimed that an unstable fracture propagation up to near surface is not possible because, for example, (1) the formations between the near surface and the shale gas reservoirs are not homogeneous and (2) the horizontal total stress is higher than the vertical total stress at shallow depth, which can block the growth of the fracture along the vertical direction. However, there are still some loose worries that the fractures might propagate too fast and unstably [10]. Osborn et al. [11] investigated the methane concentrations in the drinking aquifers for the active and inactive areas of shale gas production, and found that groundwater was contaminated around the active area of the gas production, where methane

* Corresponding author at: Harold Vance Department of Petroleum Engineering, Texas A&M University, 3116 TAMU 407 K Richardson Building College Station, TX 77843, USA. Tel.: +1 979 845 2205.
E-mail addresses: JihoonKim@lbl.gov, jihoon.kim@pe.tamu.edu (J. Kim), GJMoridis@lbl.gov (G.J. Moridis).

possibly originated from the shale gas reservoir, based upon the isotope analysis. Zoback et al. [8] overviewed potential environmental impacts from hydraulic fracturing, for example, due to failure of the proper cementing around the wellbore casing, treatment of the proppants used for hydraulic fracturing, storage and management of chemicals and waste water. Thus, rigorous simulation of material failure and coupled flow and geomechanics is strongly suggested for more systematic and accurate analysis of gas production and hydraulic fracturing.

There are several numerical methods used for the fracturing modeling. The discrete (distinct) element method considers intact rock and fractures separately, and models fracture propagation by splitting nodes [12–14]. This method is natural because the numerical scheme follows the physical process of fracturing. This discrete element method can be suitable for small scale problems that can represent intact rock and fractures individually. However, it requires huge computational cost for large scale problems in the full 3D system. On the other hand, the extended finite element method and the enhanced assumed strain method are based on the continuum approach [15,16]. These methods use discontinuous interpolation functions for discontinuous displacement in order to represent fractures, not requiring the remeshing procedure. Yet, the applications in the full 3D problems result in considerable complexities and huge coding effort. In reservoir engineering, Ji et al. [17] proposed a numerical algorithm for hydraulic fracturing, which is based on tensile strength, incorporating poromechanical effects. Dean and Schmidt [18] fundamentally employed the same fracturing algorithm of Ji et al. [17], while they used different criteria of the fracture propagation based on rock toughness of fracture mechanics. Yet, hydraulic fracturing that can consider dynamic interrelations between flow and geomechanics has still been little investigated, although tight coupling between them is necessary to consider, particularly for the cases of hydraulic fracturing and gas production in shale gas reservoirs.

In this study, we focus on physical responses related to hydraulic fracturing, while those during production are analyzed elsewhere [19]. For hydraulic fracturing, creation, propagation, and the aperture of the fractures depend on several factors such as initial reservoir condition of saturation, injected fluid pressure or injection rate, geomechanical moduli, heterogeneity, criteria of tensile failure, a type of fluid within the fractures, and permeability models. We will analyze fracture propagations induced by hydraulic fracturing for Marcellus shale gas reservoirs with various test cases.

2. Shale gas reservoirs

We describe a fracturing scenario, initial condition, and tensile strength of shale gas reservoirs in this section. Hydraulic fracturing in shale gas reservoirs is usually performed with several horizontal wells, where the direction of the horizontal wells is typically parallel to that of the compressive minimum principal total stress, S_h. Then artificial fractures created by hydraulic fracturing are normal to the direction of S_h. Many fracturing stages per horizontal well can be performed to maximize fractured areas [8].

This fracturing scenario has been applied to shale gas plays such as Barnett shale, Woodford shale, Marcellus shale, Eagle Ford shale. Among them, much attention has currently been paid to vertical fracture propagation in Marcellus shale, related to possibility of contamination in drinking water [11]. Fig. 1 shows real data of the microseismic signals (inferred fracture propagation) in Marcellus shale [6]. From the figure, all the fractures are below 4500 ft (1372 m) in depth, 3500 ft (1067 m) lower than the deepest fresh water wells, which are likely deeper 'aquifers', and the lowest injection depth is approximately 5000 ft (1524 m) in depth. The fractures propagated preferably upward, but, from the
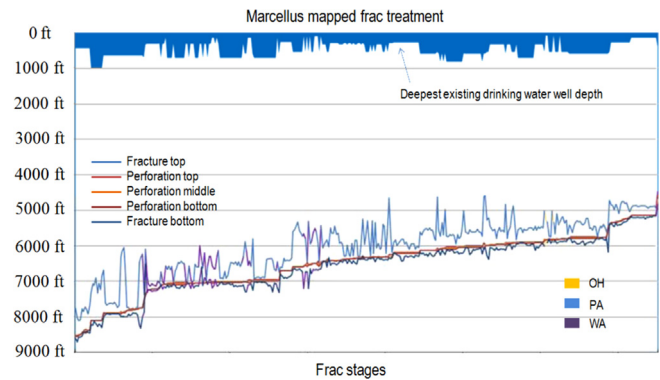

Fig. 1. Real data for the fracture propagations of Marcellus shale [6].

data, the fracture propagations do not seem dangerous when we consider the distance between fracture tops and the water well bottoms. Among the fractures whose tops are close to the surface, their maximum vertical lengths from the center of perforation are approximately no greater than 460 m.

Overburden stress, S_V, can be estimated by density of geomaterials, ρ_b. For example, the density of Marcellus shale ranges from 2200 kg/m^3 to 2600 kg/m^3 [20,21]. For horizontal stresses (i.e., S_H and S_h), where S_H is the compressive maximum horizontal principal total stress, there are several equations that relate S_V to S_H and S_h [22]. In this study, we use one of the equations as follows:

$$\frac{S_h}{S_V} = \frac{0.15}{h_z} + 0.65, \quad \frac{S_H}{S_V} = \frac{0.27}{h_z} + 0.98, \tag{1}$$

where h_z is the depth in km. When considering a simulation domain from $h_z = 1.0$ km, we approximately have $S_h = 0.8 \times S_V$ and $S_H = 1.2 \times S_V$.

For reservoir temperature, we use 0.025 °C/m of the geothermal gradient, used for normal subsurface environments and reservoirs [23]. Then, the temperature of a shale gas reservoir at 1.35 km in depth can be estimated to be 58.5 °C, when the surface temperature is 25.0 °C.

Geomechanical properties of shale gas reservoirs vary within a wide range. According to Sondergeld et al. [21], Young's modulus ranges approximately from 9 GPa to 70 GPa for the confining pressure between 10 MPa and 20 MPa, and from 7 GPa to 25 GPa for the confining pressure between 20 MPa and 30 MPa. Poisson's ratio varies from 0.1 to 0.38 for the confining pressure between 10 MPa and 20 MPa, and from 0.1 to 0.25 for the confining pressure between 20 MPa and 30 MPa. From Eq. (1), the confining pressure at $h_z = 1.0$ km is between 21.6 MPa and 25.5 MPa, and thus the corresponding Young's modulus and Poisson's ratio are around 10 GPa and 0.2, respectively.

It seems that geomechanical properties of oil shale are similar to those of shale gas reservoirs, as described below. According to Eseme et al. [24], the geomechanical properties depend on a degree of organic content and temperature, T. As the organic carbon content (or grade) and temperature increase, Young's modulus and rock strength decrease. For example, Young's modulus, E, ranges from 6.0 GPa to 12.0 GPa around $T = 58.5$ °C. Poisson's ratio, ν, ranges from around 0.2 to 0.4, depending on temperature and the organic content. Tensile strength of oil shale, T_c, ranges from 5.0 MPa to 10.0 MPa, where it is determined from a tension test such as the Brazilian test. From the similarity between oil shale and shale gas reservoir, we can infer tensile strength of Marcellus shale from data of oil shale, although there is no available data of tensile strength in Marcellus shale.

Since we focus on risk analysis of fracture propagation, we take geomechanical values and initial conditions that are favoable to fracturing. Specifically, we use $\rho_b = 2200$ kg/m^3 for
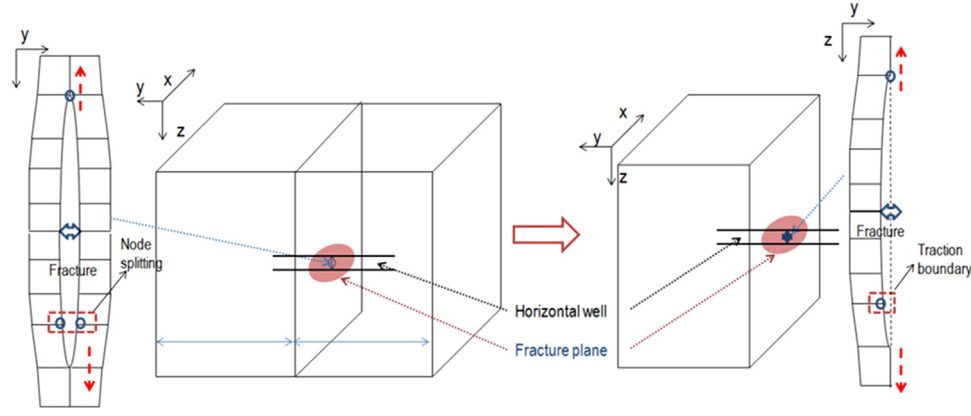
Fig. 2. Schematics of hydraulic fracturing in 3D [25]. Left: general type of planar fracturing. Right: vertical propagation of a fracture reduced from a general planar fracture.

low S_h, $E = 6$ GPa and $T_c = 4.0$ MPa to intensify the impact of geomechanics.

When two or more fluid phases are present, the physical responses are much complex because of relative permeability, saturation, significant changes in absolute permeability and geomechanical properties, and gravity segregation. We will identify the complex physics with numerical examples later in this paper.

3. Modeling of hydraulic fracturing

3.1. Tensile and shear failure

We briefly describe the modeling on hydraulic fracturing presented in Kim and Moridis [25]. Fig. 2 shows a schematics of hydraulic (tensile) fracturing in 3D, which can be modeled by splitting the nodes (e.g., [12]). For example, when effective stresses satisfy a tensile failure condition of material, one node is split into several nodes, creating a fracture. In this study, we employ a fracturing condition of tensile failure, written as

$$t_n \geq T_c, \tag{2}$$

where t_n is the normal effective stress acting on a fracture plane, just as used in Ji et al. [17].

Even though the concept of the modeling in hydraulic fracturing seems simple, it requires updating the connectivity of data structures among elements, nodes, and faces between elements, every time when tensile failure occurs, which results in significant complexity and modification in geomechanics simulators as well as huge computational cost.

On the other hand, when only considering vertical propagation of fractures, we can use no horizontal displacement condition at the surface that contains the vertical fractures. Then, we can modify the 3D general planar fracturing problems, locating the surface of the vertical fractures at the outer boundaries, as shown in the right of Fig. 2. As a result, the update of the data structure becomes straightforward in numerical simulation, because tensile fracturing occurs only at the boundaries of the domain. Instead of splitting the internal nodes, we simply change the essential (Dirichlet) boundary condition to the traction (Neumann) boundary condition [17], when tensile fracturing occurs. Effort in updating the data structures and in modifying the geomechanics codes is significantly reduced.

We also account for shear failure simultaneously during hydraulic fracturing, for example, introducing the Mohr–Coulomb

model as follows:

$$f = \tau'_m - \sigma'_m \sin \Psi_f - c_h \cos \Psi_f \leq 0, \qquad g = \tau'_m - \sigma'_m \sin \Psi_d - c_h \cos \Psi_d \leq 0, \tag{3}$$

$$\sigma'_m = \frac{\sigma'_1 + \sigma'_3}{2} \quad \text{and} \quad \tau'_m = \frac{\sigma'_1 - \sigma'_3}{2}, \tag{4}$$

where f and g are the yield and plastic potential functions, respectively. σ'_1, σ'_2, and σ'_3 are the maximum, intermediate, and minimum principal effective stresses, respectively, in which tensile stress is positive. c_h, Ψ_f, and Ψ_d are the cohesion, friction angle and dilation angle, respectively.

It should be noted that when a geomechanical problem is solved, the boundary conditions of geomechanics for tensile failure are not prescribed but dependent on the solutions of geomechanics. On the other hand, shear failure yields material nonlinearity, while the boundary conditions are still prescribed and unchanged. Both failure conditions result in nonlinear geomechanical problems.

3.2. Coupling of fluid–heat flow and geomechanics

Fluid flow and heat flow are modeled based on the conservation laws for fluid mass and heat, respectively. For geomechanics, we employ quasi-static mechanics that conserves linear momentum, as follows:

$$\text{Div } \boldsymbol{\sigma} + \rho_b \boldsymbol{g} = \boldsymbol{0}, \tag{5}$$

where Div is the divergence operator, $\boldsymbol{\sigma}$ is the total stress tensor, ρ_b is the bulk density, and $\boldsymbol{g}$ is the gravity vector. Tensile stress and strain are positive in this study.

For multiphase-multicomponent fluid and heat flow, we write the governing equation as [26]

$$\frac{d}{dt} \int_\Omega m^k \, d\Omega + \int_\Gamma \mathbf{f}^k \cdot \mathbf{n} \, d\Gamma = \int_\Omega q^k \, d\Omega, \tag{6}$$

where the superscript k indicates the fluid component or heat. $d(\cdot)/dt$ means the time derivative of a physical quantity $(\cdot)$ relative to the motion of the solid skeleton. $\mathbf{f}^k$ and q^k are its flux and source terms on the domain Ω with a boundary surface Γ, respectively, where $\mathbf{n}$ is the normal vector to the boundary.

In space discretization, we use the finite volume method, also called the integral finite difference method, for fluid–heat flow, and the finite element method for geomechanics, respectively. We developed an in-house geomechanics simulator, namely ROC-MECH, coupled to a fluid and heat flow simulator for shale gas reservoirs, TOUGH+RealGasH2O, in order to simulate coupled flow and geomechanics such as thermo-poro-mechanical effects

and hydraulic fracturing. The coupled simulator, shortly T+M, based on the mixed finite element and finite volume methods, can provide more stable solutions in space discretization, when compared with the finite element method for both flow and geomechanics [27,28]. In time discretization, T+M employs the backward Euler method, following the flow simulator.

For thermo-poro-mechanics, we employ the fixed-stress sequential implicit method, described in Kim et al. [29], which can provide numerical stability in solving thermo-poro-mechanics. By this method, we first solve fluid–heat flow, fixing the total stress field. Then, geomechanics is solved, based on the updated flow variables from the flow step. At the geomechanics step, we update the traction boundary along the fracture surface from fluid pressure and saturation solutions for tensile failure every iteration, also taking the return mapping for shear failure at the same time.

For further numerical stability, we control time step sizes that can cause no fracturing at least once at the next time of any events of tensile fracturing, because permeability is a strong function of failure status, varying from nanodarcy to Darcy. By this control method, we can ensure a time-dependant fracturing during simulation.

We employ the multiple porosity (continuum) model in thermo-poro-mechanics, which can allow more realistic flow simulation for the fracture and rock matrix systems [19,29]. Since fracturing induces a fracture–rock matrix system from the rock matrix only, we employ the dynamic dual continuum approach, shown in Fig. 3. In the dual or multiple interacting continuum (MINC) model, fluid flows through the fracture medium over the domain. On the other hand, the rock matrix medium stores fluid and conveys it to the fracture medium. We may have several rock matrix media for accurate modeling of fluid–heat flow. For coupling in pore-volume in multiple porosity, the fixed-stress split yields

$$\Delta \Phi_l^n = \left(\frac{\alpha_l^2}{K_l} + \frac{\alpha_l - \Phi_l^n}{K_s} \right) \Delta p_l^n + (3\alpha_{T,l}\alpha_l) \Delta T_l^n - \frac{b_l}{\eta_l} \Delta \sigma_v^{n-1}, \quad b_l = -\left(\frac{\alpha \eta}{K} \right)_l,$$

$$(7)$$

where Φ (Lagrange's porosity, also called reservoir porosity) is defined as the ratio of the pore volume in the deformed configuration to the bulk volume in the reference (typically initial) configuration. The subscript l indicates a material in a gridblock, such as a fracture or rock matrix medium. p_l, T_l, α_l, $\alpha_{(T,l)}$, η_l, and K_l are the pressure, temperature, Biot coefficient, thermal dilation coefficient, volume fraction, and drained bulk modulus for material l, respectively. $\alpha_l = 1 - K_l/K_l^s$, where K_l^s is the intrinsic solid grain bulk modulus of material l. σ_v is the total (volumetric) mean stress in the gridblock.

The superscript n indicates time level in time discretization. $\Delta(\cdot)^n = (\cdot)^{n+1} - (\cdot)^n$.

Validation of T+M is shown elsewhere [25], matching numerical results with the analytical solutions of poromechanics (Terzaghi's and Mandel's problems [30,31]), of fracture opening [32], and of viscosity- and toughness-dominated fracture propagations [12,33,34].

4. Numerical simulation

The propagation of fractures is determined by several factors. According to Fisher and Warpinski [6], fracture propagation is highly affected by initial distributions of reservoir pressure and total stress, and heterogeneity of geological formations. Dean and Schmidt [18] indicated that the fracture propagation is also considerably sensitive to tensile strength of geomaterials. Extending the previous studies, we perform numerical investigation on critical factors that affect fracture propagation induced by hydraulic fracturing.

We select the properties and initial conditions of flow and geomechanics, based on the previous section of Marcellus shale. We use 6.0 GPa of Young's modulus and 0.3 of Poisson's ratio, respectively. The tensile strength of the shale for the reference case is 4.0 MPa. These geomechanical properties are chosen for conservative risk analysis of fracture propagation. Initial reservoir pressure is 17.10 MPa at 1350 m in depth with the 12.44 kPa/m gradient. Initial temperature is 58.75 °C at 1350 m in depth with the 0.025 °C /m geothermal gradient. From the previous estimates of the total stress distribution, the initial total principal stresses are 36.40 MPa, and 23.30 MPa, and 29.12 MPa at 1350 m in depth in x, y, and z directions, respectively, where the corresponding stress gradients are 27.0 kPa/m, 17.59 kPa/m, and 21.57 kPa/m, respectively.

We consider gravity with 2200 kg/m^3 of the bulk density. There are no horizontal displacement boundary conditions at sides, except the fractured nodes, and have no displacement boundary at the bottom. The domain of geomechanics is discretized with 50, 5, 50 gridblocks in x, y and z directions, respectively, where the x–z plane is normal to S_h. The sizes of the gridblocks in the x and the z direction are uniform, i.e., $\Delta x = \Delta z = 3$ m. The sizes of the gridblocks in the y direction are non-uniform, i.e., 0.1 m, 0.5 m, 3.0 m, 10.0 m, 20.0 m.

Once tensile fracturing occurs, for permeability of the created fracture, we employ nonlinear permeability motivated by the
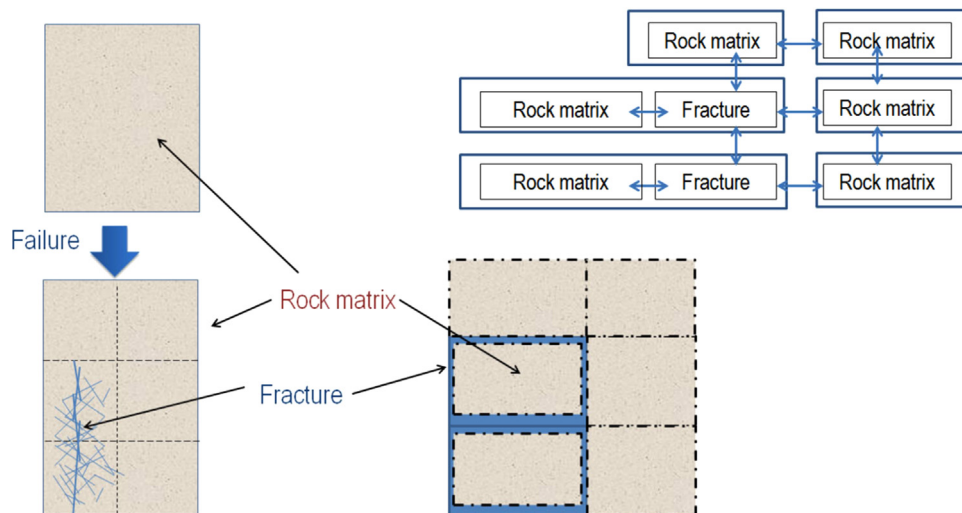

Fig. 3. Left: a schematic diagram of a fracture–rock matrix system after fracturing. Right: a conceptual model of the dynamic dual continuum model.

cubic law [35,36], written as, for an example of single water phase

$$Q_w = a_c \frac{\omega^{n_p}}{12\mu_w} H(\mathbf{Grad}\, p \quad \rho_w \mathbf{g}), \tag{8}$$

where ω is the fracture opening (width, also called the aperture). H is the fracture plate width, $\mathbf{Grad}$ is the gradient operator, and $\mathbf{g}$ is the gravity vector. Q_w, μ_w and ρ_w are flow rate, viscosity, and density of water, respectively. a_c is the correction factor reflecting the fracture roughness, as used in Nassir et al. [37]. We use $n_p = 3.0$, and $a_c = 0.14$. We calculate the fracture permeability of a gridblock based on harmonic average of the permeabilities at the grid points near the gridblock, where the cut-off value (minimum permeability) of the fracture is the same as the permeability induced by shear failure, 60 mD.

Once failure occurs, we change the single porosity model to the double porosity. Fracture and rock matrix volume fractions are 0.1 and 0.9, respectively. The reference fracture porosity is 0.9, when the fracture is created. Then the porosity varies after the creation of the fracture, showing poromechanical effects. Biot's coefficient is 1.0. We inject gas at ($x=75$ m, $z=-1440$ m) with $Q_g = 8.0$ kg/s injection rates. We assume that the injected gas has the same physical properties as shale gas for simplicity. We choose gas injections as a reference case for conservative risk assessment of fracture propagation, because gas has higher mobility in shale gas reservoirs than water does, and it can yield fast fracturing, which will be identified in the following numerical tests.

For modeling relative permeability and capillarity in this study, we use a modified version of Stone's relative permeability model [38] and the van Genutchen capillary pressure model [39], respectively, written as

$$k_{rJ} = \max\left\{ 0, \min\left\{ \left(\frac{S_J - S_{ir,J}}{1.0 - S_{ir,w}} \right)^{n_k}, 1 \right\} \right\}, \tag{9}$$

$$P_c = \Pi_c \left((S^e)^{-1/\lambda_p} - 1 \right)^{1-\lambda_p}, \quad S^e = \frac{S_w - S_{ir,w}}{1 - S_{ir,g} - S_{ir,w}}, \tag{10}$$

where k_{rJ}, $S_{ir,J}$, and n_k are relative permeability of phase J, irreducible saturation of phase J, and the exponent that characterizes the relative permeability curve, respectively. P_c, λ_p and Π_c are capillary pressure, the exponent that characterizes the capillary pressure curve, and the capillary modulus, respectively. Then, for the reference case, we take $S_{ir,w} = 0.08$, $S_{ir,g} = 0.01$, and $n_k = 4.0$ for relative permeability, and $\lambda_p = 0.45$, $S_{ir,w} = 0.05$, $S_{ir,g} = 0.0$, and $\Pi_c = 2.0$ kPa for capillarity, where smaller $S_{ir,w}$ and $S_{ir,g}$ of the capillarity model are chosen in order to prevent unphysical behavior [40].

For multiphase flow coupled with geomechanics, we employ the equivalent pore–pressure concept [41], not using the average pore–pressure concept. When strong capillarity exists, the equivalent pore–pressure provides high accuracy, whereas the average pore–pressure may cause large numerical errors [42].

We vary the injection rate, types of injection fluid, initial saturation, relative permeability, Young's modulus, Poisson's ratio, intrinsic fracture permeability, and heterogeneity of tensile strength, and investigate fracture propagation as well as flow and geomechanical responses.

4.1. Gas injection: reference case

Fig. 4 shows vertical fracture propagation at the x–z plane due to tensile failure. At initial time, a small fracture is created. However, the fracture grows horizontally and vertically because of continuous injection of gas, which contributes to additional geomechanical loading normal to the fracture. During hydraulic fracturing in this simulation, we obtain a finite length of the fracture. This implies that the fracture propagation is stable and can be controlled by injection time, equivalently injection rate. It

should be noted that the fracture propagates upward much more than downward, because S_h at the initial condition decreases as the depth decreases, yielding higher net pressure in fracturing. From the right of Fig. 4, as the net pressure is higher at the shallow depth, the fracture opening becomes larger at the top of the fracture than at the bottom.

We find clear differences in pressure between inside and outside the fracture, as shown in Fig. 5 (a). The fracture opened by tensile failure yields high permeability of the fracture, and thus the pressure loss within the fracture is almost negligible (i.e., hydro-static pressure), because of high fracture permeability and high mobility of gas within the fracture. The high pressure gradient at the fracture tip, which is almost discontinuous, is fundamentally due to the considerable difference in permeability between the fracture and the reservoir. Fig. 5 (b) shows saw-toothed evolution of pressure, because, when fracturing occurs by pressurization of fluids within the fracture, the fracture volume increases immediately, inducing instantaneous pressure drop due to fluid expansion and fast pressure diffusion.

At early time, this saw-toothed (oscillatory) behavior is much distinct, because of small volume of the fracture, but, as the fracture volume becomes large, the magnitude of the oscillation becomes small. We also observe smaller fracture opening at the injection point at 16.0 s than that at 4.0 s, from the right of Fig. 4, mainly because pressure within the fracture becomes lower. Specifically, Fig. 5(c) and (d) shows variation of the fracture width at the injection point and uplift at ($x=75$ m, $z=-1350$ m), the top of the domain, respectively. The oscillations originate from the oscillation of pressure (Fig. 5 (b)). The fracture becomes open and closed repeatedly, depending on fracturing status and pressure. In Fig. 5(d), we also find uplift of the top because of injection of fluid.

It should be noted that responses of geomechanics are instantaneous due to quasi-statics (i.e., elliptic partial differential equation (PDE)), while those of fluid pressure are slower (i.e., parabolic PDE), depending on pressure diffusivity. Thus, two different time scales cause the dry zone (i.e., fluid lag) between the fracture tips and the pressurized fluid, particularly for low permeable reservoirs. According to Adachi et al. [43], a fluid lag is likely for lower permeable reservoirs, for example, less than 100 mD, while an invaded zone can occur for higher permeable reservoirs greater than 1.0 Darcy.

Fig. 5(e) and (f) shows evolution and distribution of $\sqrt{J_2}$ at the x–z plane, another measure of effective shear stress. J_2 is the second stress invariant of the effective deviatoric stress. From the figure, shear stress increases during simulation and high shear stresses are located near the fracture tips. This implies that shear deformation mainly occurs around the fracture tips. The shear deformation is also identified in the right of Fig. 4, which shows the large gradient of displacement around the fracture tips.

The effective stresses at the domain at early and late times are also plotted, based on the Mohr–Coulomb model (Fig. 5 (g) and (h)). We use 4.0 MPa of cohesion, lower than that in Eseme et al. [24] for a given temperature, for conservative risk analysis. We also employ 28.9° (=0.5 rad) of friction and dilation angles, consistent with the values in Eseme et al. [24]. From Fig. 5(g) and (h), all the effective stresses are positioned below the failure line during simulation (i.e., until 600 s), indicating that no shear failure occurs. The effective stresses become closer to the failure line at late times, and some of σ_n''s are positive because of tensile effective stress induced by fluid injection. When the fracturing operation takes longer or a weaker formation exists, we may potentially face shear failure later.

4.2. Water injection

We change the injection fluid from gas to liquid water. All the conditions are the same as previous (e.g., $S_w = 0.1$ over the domain).
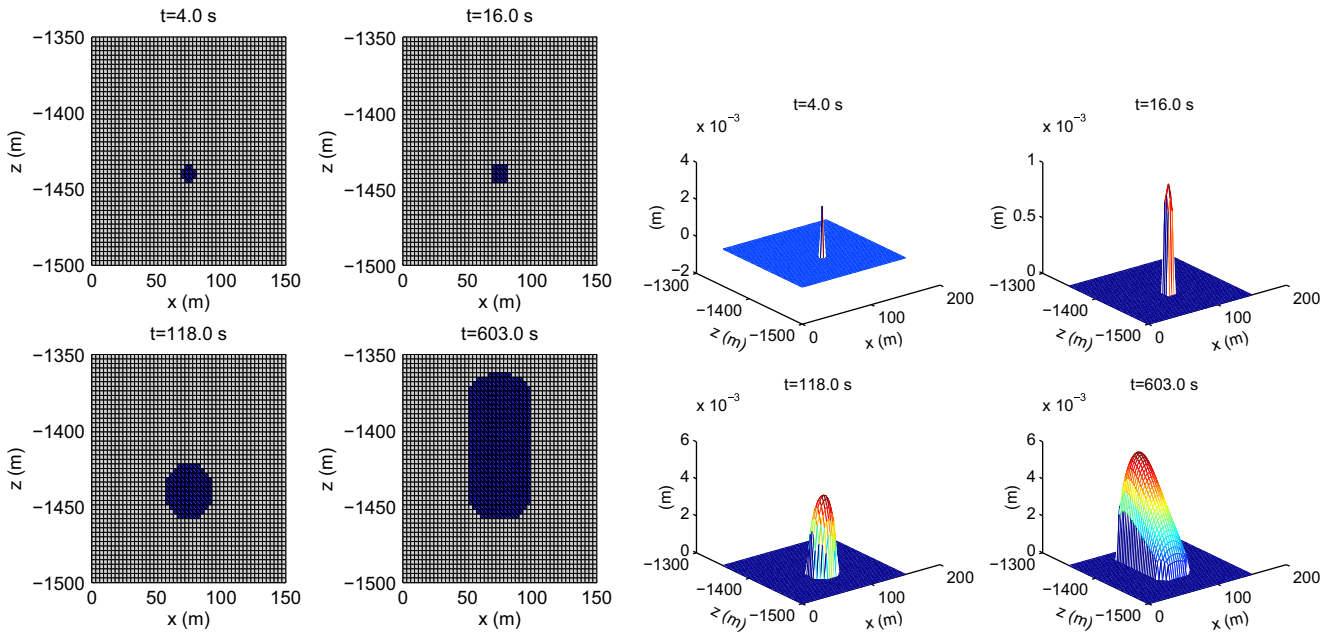
Fig. 4. Gas injection reference case. Left: vertical fracture propagation in the *x–z* plane. Right: the fracture openings.
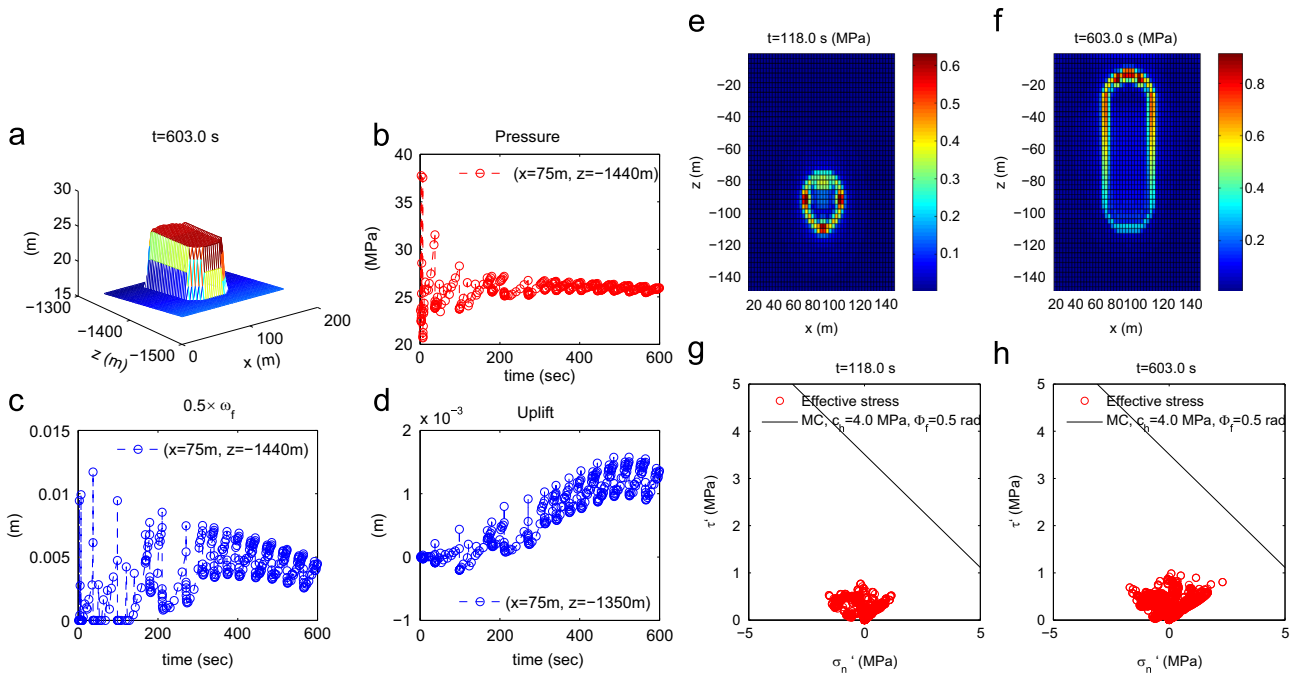

Fig. 5. Left: (a) pressure distribution at *t*=603 s, (b) evolution of pressure at the injection point, (c) variation of the fracture opening at the injection point, (d) uplift at the top of the domain. Right: (e) and (f) distributions of $\sqrt{J_2}$ at the *x–z* plane, (g) and (h) the Mohr–Coulomb plot of effective stress.

From Fig. 6(a) and (b), fracture propagation becomes much slower, compared with the reference case (i.e., gas injection), because water injection induces very slow pressurization, when gas is dominantly saturated. When we consider no vertical fracturing at $x=75$ m between 16 s and 118 s, evolution of pressure at $x=75$ m, shown in Fig. 6(c), indicates that pressurization and pressure diffusion are slow, compared with the reference case, because of low relative permeability of liquid water. In Fig. 6(d), water saturation at ($x=73.5$ m, $z=-1435.5$ m), one of the fractured gridblocks, increases slowly from water injection.

We change the initial water saturation of the reservoir from $S_w=0.1$ to $S_w=0.9$ with water injection. This condition can approximate fracture propagation within a water-saturated formation above shale gas reservoirs. Evolution of pressure at $x=75$ m shown in Fig. 6

(g) implies that due to high saturation of water, pressurization and pressure diffusion become much faster, compared with low initial water saturation. Accordingly, fracturing becomes much faster, having larger fractures, as shown in Fig. 6(e) and (f).

In Fig. 6(h), water saturation decreases when fracturing occurs, particularly at early time. In addition, water and gas coexist even near the injection well. When fracturing occurs, reservoir gas (i.e., shale gas) flows into the dry zone at the fracture tips immediately because of high mobility of gas and a thin fracture aperture compared with the fractured length. Then water injection pressurizes both gas and water within the fracture, which induces further fracturing. Thus, the fracturing fluids are not only water but also shale gas. Furthermore, the fracture volume can be larger than the injection fluid volume,
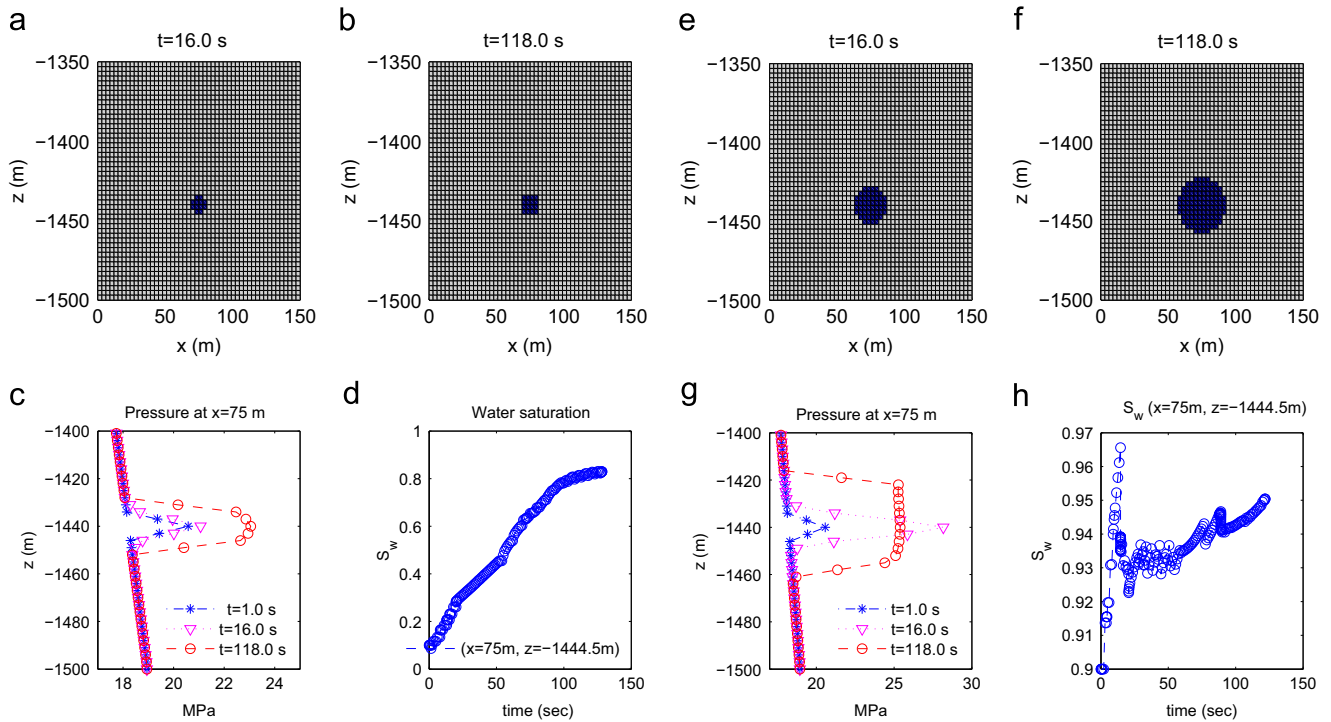
Fig. 6. Fracture propagation for water injection, pressure evolution at $x=75$ m, and evolution of water saturation, when the initial water saturations are 0.1 (left figure) and 0.9 (right figure), respectively.

because of coexistence of water and gas. Thus, estimation of the fracture volume only from the injected fluid volume, for example, claimed by Fisher and Warpinski [6], might underestimate the vertical fracture propagation.

4.3. Initial saturation and relative permeability

To investigate the effects in initial saturation and relative permeability, we change the initial water saturation of the reference case from $S_w=0.1$ to $S_w=0.6$, and the exponent of relative permeability from 4.0 to 2.0, which allows higher mobility of water at low water saturation. Gas is injected, same as the reference case.

In this test, we obtain large fracturing, compared with the reference case, when considering the fractured areas and nodes, as shown in Fig. 7(a)–(c). Even though the initial condition is not much close to the condition of Marcellus shale reservoirs, the numerical results indicate that accurate initial condition and precise relative permeability model are necessary for accurate prediction in geomechanical responses during hydraulic fracturing.

Fig. 7(d) shows evolution of water saturation at ($x=73.5$ m, $z=-1435.5$ m) and water saturation distribution at $t=301$ s. Interestingly, water saturation decreases at early times because of gas injection. Then, it increases again up to 0.9 due to gravity segregation between gas and water within the fracture. High fracture permeability induces fast gravity segregation. In the right of Fig. 7, we identify the gravity segregation, where water is concentrated at the bottom area while gas is at the top. In this figure, we observe that gas and water coexist within the fracture, just like the previous water injection test. We here find that the created fracture volume is higher than the volume of the injection fluid, and that, accordingly, simple estimation based on the volume of the injection fluid underestimates the fracture volume and fracture propagation.

4.4. Injection rate

We increase the injection rate of gas from 8.0 kg/s of the reference case to 16.0 kg/s. Fig. 8(a) and (b) show faster fracture propagation, when compared with the reference case. When the injection increases by a factor of two, fracturing becomes faster almost by a factor of two. This nearly linear relation can also be found in a different horizontal stress condition of Kim and Moridis [25], where fracturing becomes slower by a factor of 10 when the injection decreases by a factor of 10. In Fig. 8(c), evolution of the fracturing opening at $t=301$ s is similar to that of the reference case at $t=603$ s, except time scale. The similarity is also found in evolution of pressure, as shown in Fig. 8(d), where the pressure at the injection point is oscillatory, just like the reference case. However, because of shorter injection time, more fracturing occurs in this case than that for the reference case, because of smaller leak-off to the reservoir formation. In this test case, approximately, 450 nodes are fractured, while about 420 nodes are fractured for the reference case. We also observe that the peak pressure at the injection point is 62 MPa, shown at early times, because of fast injection. The peak pressure is much higher than that from the reference case, 37 MPa.

4.5. Heterogeneity in tensile strength

We modify the reference case, assigning 10 MPa of tensile strength to the layers between 1380 m and 1410 m in depth. This case is taken as a scenario that a strong formation may be located between shale gas reservoirs and near surface aquifers (or aquitards). From Fig. 9(a) and (b), the strong formation blocks fracturing in the vertical direction, and instead fracturing occurs horizontally, changing the fracturing direction. This result is consistent with the arguments in other studies such as Fisher and Warpinski [6] and King [44] that heterogeneity of fracturing barriers, heterogeneous S_h, and leak-off can limit vertical fracturing. Fig. 9(c) shows that the fracture also opens in the horizontal direction.
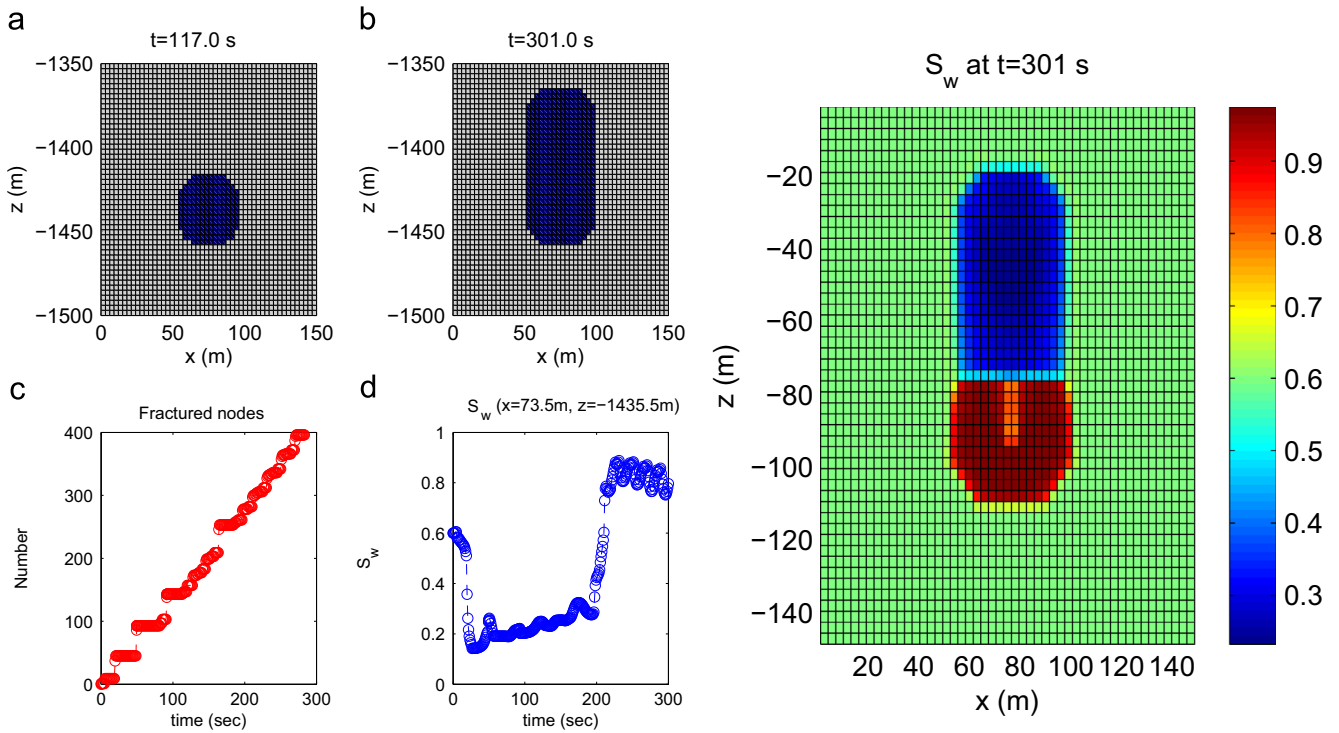
Fig. 7. Left: (a) and (b) fracture propagation with gas injection when initial water saturation is 0.6 and $n_p = 2.0$, (c) the number of the fractured nodes, and (d) evolution of water saturation. Right: distribution of water saturation.
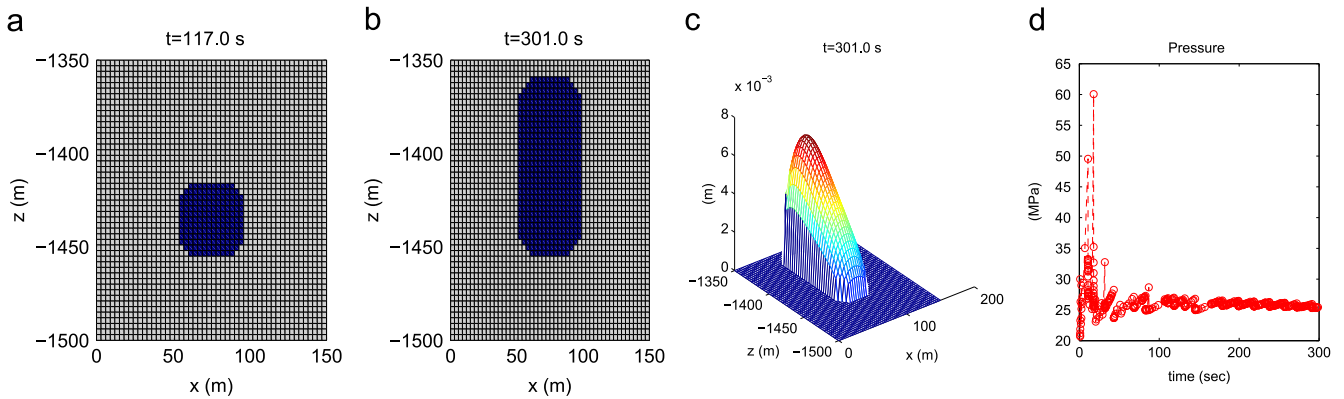

Fig. 8. (a) and (b) vertical fracture propagation at the x–z plane due to tensile failure with $Q_g = 16.0$ kg/s, (c) the fracture opening at $t = 301$ s, and (d) evolution of pressure at the injection point.
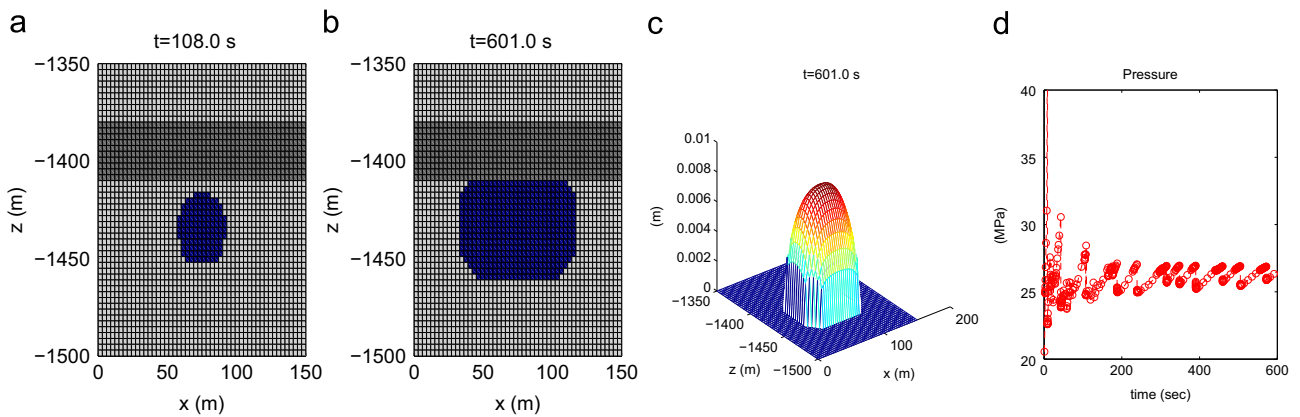

Fig. 9. (a) and (b) vertical fracture propagation at the x–z plane when the layers between 1380 m and 1410 m in depth (dark gray area) have high tensile strength, (c) the fracture opening, and (d) evolution of pressure at the injection point.
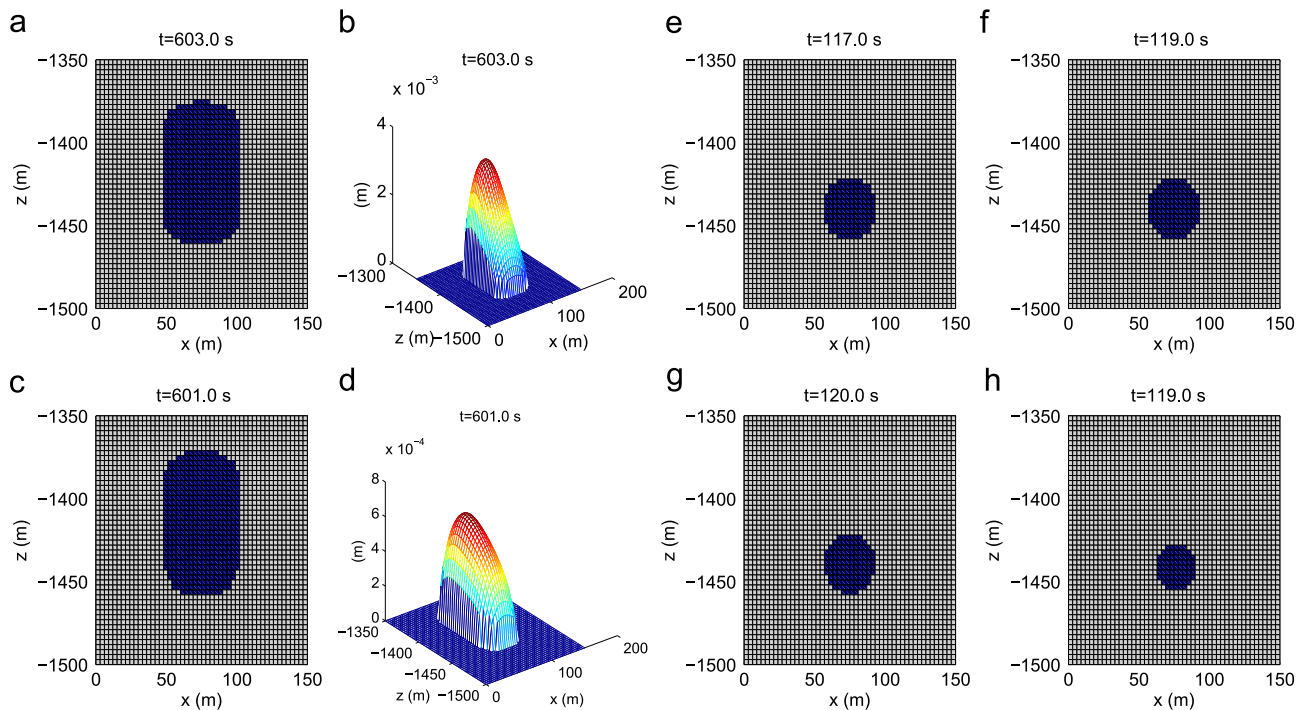
Fig. 10. Left: vertical fracture propagations and fracture openings at the x–z plane for $E = 10.0$ GPa ((a) and (b)), for $E = 60.0$ GPa ((c) and (d)). Right: fracture propagations for $\nu = 0.1, 0.2, 0.35, 0.4$ ((e), (f), (g), and (h), respectively).

Fig. 9(d) shows the pressure behavior, which is somewhat different from those of the reference case. At the late times after the fracturing direction changes, we observe slower fracturing frequencies, when comparing the reference case, because the pressure required for fracturing, around 27 MPa, is higher than the pressure of the reference case, 26 MPa. Fracturing occurs at the deeper depth where S_h is higher, resulting in higher fluid pressure for fracturing than that of the reference case.

4.6. Young's modulus, Poisson's ratio, permeability, and tensile strength

We take 10 GPa of Young's modulus, increased from 6 GPa of the reference case. In Fig. 10(a)–(b), we find that there is little difference in the fractured area between this test case and the reference case. However, the fracture widths are lower than those of the reference case, because of higher stiffness in geomechanics. For 60 GPa of Young's modulus (Fig. 10(c)–(d)), we observe slightly slower fracture propagation and smaller fracture openings than those for the reference case. When Young's modulus is high for given effective stress, deformation of porous media is small, yielding small fracture opening. Thus, lower fracture permeability induced by smaller fracture opening causes slower fluid flow, resulting in slower fracture propagation.

We also test the effects of Poisson's ratio, which covers a wide range [21,45,46]. In Fig. 10(e)–(h), although Poisson's ratio does not seem to affect fracture propagation noticeably, we find slightly less fracturing as Poisson's ratio increases, particularly for $\nu = 0.4$. This might results from the fact that, for a given Young's modulus, high Poisson's ratio decreases shear modulus, modulus of rigidity. However, it should be noted that these results are restricted to limited test cases of gas injection, and more rigorous investigation needs to be performed in the future. For example, various Poisson's ratios yield a wide range of the bulk modulus, which might result in different poromechanical effects. Water injection can yield strong poromechanical behavior because water is

incompressible, although gas injection is not much sensitive to poromechanics.

We reduce the fracture permeability by one order, having $a_c = 0.014$, when it is compared with the reference case. Even though the fracture permeability is reduced significantly, the fractured area is similar to that of the reference case, shown in Fig. 11(a) and (b). Both the cases provide extremely high permeability because of large fracture openings. The high permeability results in fast pressure diffusion sufficient for hydro-static pressure equilibrium.

We reduce tensile strength from 4 MPa to 1 MPa for a possible weaker shale gas reservoir. In Fig. 11(c) and (d), we find a stable fracture propagation for the given simulation time, although the fracture shape is different from the shape of the reference case. The low tensile strength induces more horizontal fracturing, in the x-direction, compared with the reference case.

5. Closure

We numerically investigated geomechanical responses during hydraulic fracturing operations for generalized Marcellus shale gas reservoirs. Due to existence of the dry-zone, simple estimation of the fracture volume based on the amount of injected fluid may underestimate the growth of the vertical fracture, because the injected and reservoir fluids coexist within the created fracture. Yet, from various numerical tests, hydraulic fracturing produced stable fracture propagations, supporting the argument from the real data in the previous studies, for example, no greater than 460 m of vertical fracture propagation inferred from microseismic signals. We observed saw-toothed responses, having some frequencies, because of discontinuous fracturing in time and different time scales governed by two different physics, i.e., flow and geomechanics. High effective shear stress was concentrated near the fracture tip, and shear failure might be possible for long-time simulation or weak shale gas reservoirs.
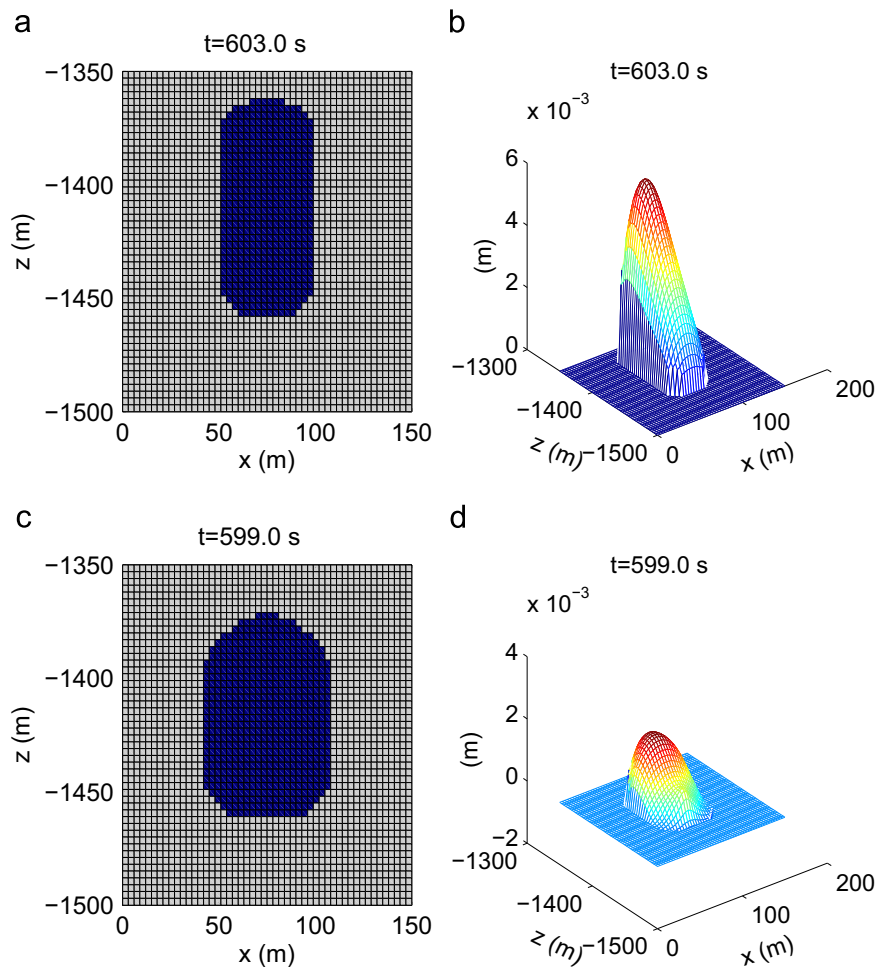
Fig. 11. Vertical fracture propagation and fracture openings at the x–z plane when the reference fracture permeability is reduced by one order ((a) and (b)), and when $T_c = 1.0$ MPa ((c) and (d)).

We found that hydraulic fracturing is affected by several factors, such as types of injection fluid, injection rate, tensile strength, intrinsic permeability, initial condition of saturation, Poisson's ratio, relative permeability models, geomechanical moduli, and heterogeneity. Gas injection generated faster fracturing in shale gas reservoirs than water injection, because of high mobility of gas. But, for high initial water saturation, water injection also provided sufficient fracturing due to fast pressurization. We identified complicated physical responses that result from multiphase flow, fracture propagation followed by nonlinear permeability, and gravity segregation between gas and water. High intrinsic and high relative permeabilities resulted in fast fluid movement of injected fluid, followed by fast fracturing. High Young's modulus and high Poisson's ratio were not favorable to fracture propagation, although they was not significantly sensitive. We found that a geological layer of high strength between near surface and above the shale gas reservoirs can limit vertical fracture propagation.

References

[1] Arthur JD, Bohmand B, Layne M. Hydraulic fracturing considerations for natural gas wells of the Marcellus shale. In: Proceedings of ground water protection council 2008 annual forum, Cincinnati; 21–24 September 2008.
[2] Jenkins CD, Boyer CM. Coalbed- and shale-gas reservoirs. J Pet Technol 2008;60(02):92–9.
[3] Kargbo DM, Wilhelm RG, Campbell DJ. Natural gas plays in the Marcellus Shale: challenges and potential opportunities. Environ Sci Technol 2010; 44(5):5679–84.
[4] Hill DG, Nelson CR. Gas productive fractured shales: an overview and update. Gas TIPS 2000;6(3):4–13.
[5] Vermylen JP, Zoback MD. Hydraulic fracturing, microseismic magnitudes, and stress evolution in the Barnett Shale, Texas, USA. In: Proceedings of SPE hydraulic fracturing technology conference, The Woodland; 24–26 January 2011.
[6] Fisher K, Warpinski N. Hydraulic fracture-height growth: real data. SPE Prod Oper 2012;27(1):8–19.
[7] Soliman MY, Boonen P. Rock mechanics and stimulation aspects of horizontal wells. J Pet Sci Eng 2000;25:187–204.
[8] Zoback M, Kitasei S, Copithorne B. Addressing the environmental risks from shale gas development. In: Worldwatch Institute briefing paper 1. Washington DC: Worldwatch Institute; 2010.

[9] Cipolla CL, Lolon EP, Rubin B. Reservoir modeling in shale-gas reservoirs. SPE Reserv Eval Eng 2010;13(04):638–53.

[10] Rahm D. Regulating hydraulic fracturing in shale gas plays: the case of Texas. Energy Policy 2011;39(5):2974–81.

[11] Osborn SG, Vengosh A, Warner NR, Jackson RB. Methane contamination of drinking water accompanying gas-well drilling and hydraulic fracturing. PNAS 2011;108:8172–6.

[12] Fu P, Johnson SM, Carrigan CR. An explicitly coupled hydro-geomechanical model for simulating hydraulic fracturing in arbitrary discrete fracture networks. Int J Numer Anal Methods Geomech 2013;37(14):2278–300.

[13] Ben Y, Xue J, Miao Q, Wang Y, Shi GH. Simulating hydraulic fracturing with discontinuous deformation analysis. In: Proceedings of US rock mechanics/geomechanics symposium, Chicago; 24–27 June 2012.

[14] Zhang XP, Wong LNY. Loading rate effects on cracking behavior of flaw-contained specimens under uniaxial compression. Int J Fract 2013; 180(1):93–110.

[15] Borja RI. Assumed enhanced strain and the extended finite element methods: a unification of concepts. Comput Methods Appl Mech Eng 2008;197:2789–803.

[16] Moes N, Dolbow J, Belytschko T. A finite element method for crack growth without remeshing. Int J Numer Meth Eng 1999;46:131–50.

[17] Ji L, Settari A, Sullivan RB. A novel hydraulic fracturing model fully coupled with geomechanics and reservoir simulation. SPEJ 2009;14(3):423–30.

[18] Dean RH, Schmidt JH. Hydraulic fracture predictions with a fully coupled geomechanical reservoir simulation. SPEJ 2009;14(4):707–14.

[19] Kim J, Moridis GJ. Gas flow tightly coupled to elastoplastic geomechanics for tight and shale gas reservoirs: material failure and enhanced permeability. SPEJ 2014;19(06):1110–25.

[20] Boyce ML, Carr TR. Lithostratigraphy and petrophysics of the Devonian Marcellus interval in West Virginia and Southwestern Pennsylvania; 2009. ⟨http://www.mapwv.gov/UnconventionalResources/marcellusLithoAndPetroPaper.pdf⟩.

[21] Sondergeld CH, Newsham KE, Comisky JT, Rice MC, Rai CS. Petrophysical considerations in evaluating and producing shale gas resources. In: Proceedings of unconventional gas conference, Pittsburgh; 23–25 February 2010.

[22] Zang A, Stephansson O. Stress field of the Earth's crust. Springer Science+Business Media B.V., Dordrecht; 2010.

[23] Fridleifsson IB, Bertani R, Huenges E, Lund JW, Ragnarsson A, Rybach L. The possible role and contribution of geothermal energy to the mitigation of climate change. In: Proceedings of IPCC scoping meeting on renewable energy sources, Luebeck; 20–25 January 2008. p. 59–80.

[24] Eseme E, Urai JL, Krooss BM, Littke R. Review of mechanical properties of oil shales: implications for exploitation and basin modeling. Oil Shale 2007; 24(2):159–74.

[25] Kim J, Moridis GJ. Development of the T+M coupled flow-geomechanical simulator to describe fracture propagation and coupled flow-thermal-geomechanical processes in tight/shale gas systems. Comput Geosci 2013;60:184–98.

[26] Pruess K, Oldenburg C, Moridis G. TOUGH2 User's Guide, Version 2.0. Berkeley, CA: Lawrence Berkeley National Laboratory; 1999.

[27] Wan J, Durlofsky LJ, Hughes TJR, Aziz K. Stabilized finite element methods for coupled geomechanics-reservoir flow simulations. In: Proceedings of SPE reservoir simulation symposium, Houston; 3–5 February 2003.

[28] Phillips PJ, Wheeler MF. A coupling of mixed and continuous Galerkin finite element methods for poroelasticity I: the continuous in time case. Comput Geosci 2007;11:131–44.

[29] Kim J, Sonnenthal E, Rutqvist J. Formulation and sequential numerical algorithms of coupled fluid/heat flow and geomechanics for multiple porosity materials. Int J Numer Meth Eng 2012;92:425–56.

[30] Terzaghi K. Theoretical soil mechanics. New York: Wiley; 1943.

[31] Abousleiman A, Cheng A, Detournay E, Roegiers J. Mandel's problem revisited. Geotechnique 1996;46:187–95.

[32] Sneddon I, Lowengrub M. Crack problems in the classical theory of elasticity. New York: Wiley; 1969.

[33] Gidley JL, Holditch SA, Nierode DE, Veatch RWJ. Recent advances in hydraulic fracturing. In: SPE monograph Series, vol. 12; 1990.

[34] Valko P, Economies MJ. Hydraulic fracture mechanics. New York: Wiley; 1995.

[35] Witherspoon PA, Wang JSY, Iwai K, Gale JE. Validity of Cubic Law for fluid flow in a deformable rock fracture. Water Resour Res 1980;16(6):1016–24.

[36] Rutqvist J, Stephansson O. The role of hydromechanical coupling in fractured rock engineering. Hydrogeol J 2003;11:7–40.

[37] Nassir M, Settari A, Wan R. Prediction and optimization of fracturing in tight gas and shale using a coupled geomechanical model of combined tensile and shear fracturing. In: Proceedings of SPE hydraulic fracturing technology conference, The Woodland; 6–8 February 2012.

[38] Aziz K, Settari A. Petroleum reservoir simulation. London: Elsevier; 1979.

[39] van Genuchten. A closed-form equation for predicting the hydraulic conductivity of unsaturated soils. Soil Sci Soc Am J 1980;44:892–8.

[40] Moridis GJ, Kowalsky MB, Pruess K. TOUGH+HYDRATE v1.0 user's manual: a code for the simulation of system behavior in hydrate-bearing geologic media. Berkeley, CA: Lawrence Berkeley National Laboratory; 2008.

[41] Coussy O. Poromechanics. Chichester, England: John Wiley and Sons; 2004.

[42] Kim J, Tchelepi HA, Juanes R. Rigorous coupling of geomechanics and multiphase flow with strong capillarity. SPEJ 2013;18(6):1591–606 Spe141268.

[43] Adachi J, Siebrits E, Peirce A, Desroches J. Computer simulation of hydraulic fractures. Int J Rock Mech Min Sci 2007;44:739–57.

[44] King GE. Hydraulic fracturing 101: What every representative, environmentalist, regulator, reporter, investor, university researcher, neighbor and engineer should know about estimating frac risk and improving frac performance in unconventional gas and oil wells. In: Proceedings of SPE hydraulic fracturing technology conference, The Woodland; 6–8 February 2012.

[45] Christensen NI. Poisson's ratio and crustal seismology. J Geophys Res: Solid Earth (1978–2012) 1996;101(B2):3139–56.

[46] Gercek H. Poisson's ratio values for rocks. Int J Rock Mech Min Sci 2007; 44(1):1–13.